Probing the Enzymatic Activity of Individual Biocatalytic fd -Viral Particles by Electrochemical-Atomic Force Microscopy

Telmo O Paiva, Kristian Torbensen, Anisha Patel, Agnès Anne, Arnaud Chovin, Christophe Demaille, Laure Bataille, Thierry Michon

Probing the Enzymatic Activity of Individual Biocatalytic *fd*-Viral Particles by Electrochemical-Atomic Force Microscopy

Telmo O. Paiva[1], Kristian Torbensen[1], Anisha N. Patel[1], Agnès Anne[1], Arnaud Chovin[1], Christophe Demaille*[1],*

Laure Bataille[2], Thierry Michon[2]*

[1]Université de Paris, Laboratoire d'Electrochimie Moléculaire, CNRS UMR 7591, F-75006 Paris, France

[2]Université de Bordeaux, Biologie du Fruit et Pathologie, INRA UMR 1332, F-33140 Villenave d'Ornon, France

* To whom correspondence should be addressed.

E-mail: demaille@univ-paris-diderot.fr ; anne@univ-paris-diderot.fr ; thierry.michon@inrae.fr

Abstract

Surface-immobilized *fd* bacteriophage particles are used as scaffolds to coassemble the redox enzyme quinoprotein glucose dehydrogenase, PQQ-GDH, and its cosubstrate, PEG-tethered ferrocene. Individual decorated *fd* phages are visualized and simultaneously functionally interrogated by Mt/AFM-SECM microscopy, an in-situ local probe correlative imaging technique, combining atomic force (AFM) and electrochemical (SECM) microscopy in a mediator tethered (Mt) configuration. The statistical distribution of catalytic activity across the *fd* population is resolved, and the correlation between the functional properties of the phages and their actual dimensions assessed. Moreover, achievement of sub-particle resolution allows the enzymatic activity of individual viruses to be spatially mapped, revealing a highly active region located in the middle of the filamentous *fd*-scaffold. Quantitative modeling shows that this "catalytic hot-spot" arises from the interplay between charge transport by electron hopping between ferrocene moieties along the viral particles, and enzymatic catalysis. The developed model also enables complete analysis of GDH kinetics at the single bioscaffold scale, revealing differences in the functional behavior of the biocatalytic viral particles when addressed at the ensemble or at the single particle scale.

Keywords: Single entity electrochemistry, PQQ-GDH, Bioscaffolding, Nanoparticle enhanced bioelectrocatalysis, Virus nanotechnology

Introduction

It is increasingly recognized that immobilizing enzymes onto, or within, scaffolds that are tens to hundreds of nanometers in size (nanoscaffolds) can enhance enzymatic activity, compared to when the enzyme molecules are dispersed in solution or immobilized onto non-nanostructured surfaces.[1–4] This catalytic enhancement has been observed for many different types of enzymes, such as hydrolases,[2,5] proteases,[6,7] or even redox enzymes,[3,8] assembled onto or entrapped within nanoscaffolds of various kinds, ranging from inorganic nanoparticles to bioscaffolds.[9,10] Amongst the latter, DNA nanostructures,[11–14] and more particularly DNA origamis,[15] offer unmatched control of enzyme placement, and have frequently been used to reconstitute enzymatic cascades,[10,16–20] that often displayed improved catalysis.[10,21,22] This enhancement has generally been attributed to efficient channeling of metabolites between the enzymes. However, it was recently demonstrated that it can simply be due to the confinement of the enzymes onto the DNA nanostructures, i.e. to scaffolding itself.[10,21,22]

Virus particles from plants, as well as bacteriophages, (both harmless to humans) are also very good candidates for bioscaffolding. They have often been employed to construct enzymatic systems, in search of catalytic enhancement and/or metabolite channeling. Enzymes were either displayed on the outer surface (capsid) of virus particles or encapsulated inside.[23–35] The ability of virus-based nanoscaffolds to enhance, or at least protect, enzymatic catalysis has been demonstrated in many instances.[25,26,29,32,34]

Although the phenomena of scaffolding-induced catalytic enhancement has been widely observed, a full understanding of its underlying mechanisms is still lacking.[36] Such fundamental knowledge is vital for developing artificial scaffolded enzymatic systems that display improved performances, in order to engineer more efficient bioreactors, more sensitive biosensors, or more powerful biofuel cells.[4,10,37–39] To this aim, model, organized, mono- and multi- components enzymatic systems have to be assembled onto well-defined nanoscaffolds and their catalytic behavior thoroughly studied.[10] It is also important that novel experimental approaches are proposed for an in depth exploration of the catalytic response of scaffolded enzymatic systems.

Of particular interest is the development of new experimental tools enabling investigations to go beyond the "ensemble scale" of the kinetic characterization methods used in the vast majority of studies on catalytic enhancement, where catalysis is typically probed at the scale of millions of copies of scaffolds dispersed in solution. Indeed, being able to address the catalytic behavior of *individual* enzymatic scaffolds could yield valuable information, which are otherwise averaged-out in ensemble measurements. For example, such is the case of the statistical distribution of the enzymatic activity across the scaffold population, a fundamental parameter only accessible by single-particle approaches. Moreover, since nanoscaffolds unavoidably display some degree of topological diversity (folding, shape, size), it would also be most interesting to be able to relate the activity of individual enzyme-bearing scaffolds to their actual spatial conformation.

However, until now, functional interrogation of individual enzymatic nanoscaffolds has, to the best of our knowledge, only been achieved a hand full of times. In a pioneering paper, Carette et al. probed the catalytic response of Lipase B decorating the surface of particles of the Potato Virus X (PVX), using single molecule confocal fluorescence microscopy.[27] Later, the same technique was used to visualize and analyze the activity of single Horse Radish Peroxidase (HRP) enzyme molecules entrapped within individual chlorotic mottle virus (CCMV) viral particles.[28] More recently, total internal reflection fluorescence microscopy (TIRF) was employed to record catalytic bursts arising from single molecules of glucose-6-phosphate dehydrogenase entrapped within a DNA nanocage,[8] and of HRP decorating individual DNA origami tiles,[40,41] respectively. In all of these works, the enzyme-bearing nanoscaffolds were adsorbed onto a substrate, and the activity of single *enzyme* molecules was resolved, but simultaneous in-situ visualization of the supporting individual nanoscaffolds *themselves* was not possible. This limitation notably precluded exploring the relation between the actual structure of the surface-adsorbed scaffolds and their catalytic response.

Herein, we propose to use AFM-SECM, an in-situ local probe correlative imaging technique, combining atomic force (AFM) and electrochemical microscopy (SECM),[42–44] in an original mediator-tethered (Mt) configuration,[45,46] to selectively *trigger* and *probe* the catalytic activity of *individua*l virus

particles bearing a multicomponent system integrating a redox enzyme and its cosubstrate. The chosen system is an immuno electro-enzymatic system we recently introduced,[47] consisting of the enzyme pyrroloquinoline quinone-dependent glucose dehydrogenase (PQQ-GDH) and of polyethylene glycol (PEG)-tethered ferrocene (Fc) redox moieties, co-immuno-assembled onto *fd*-bacteriophages used as viral scaffolds. We previously demonstrated, by ensemble scale cyclic voltammetry (CV) experiments, that this Fc-PEG / GDH system displays superior catalytic performances compared to other *integrated* PQQ-GDH systems reported in literature.[47] Such a catalytic enhancement warrants analysis at the individual particle level.

Herein Mt/AFM-SECM microscopy is employed to identify and topographically map *individual* Fc-PEG / PQQ-GDH decorated virus particles immobilized on a flat SiO_2 surface, whist *simultaneously* quantifying their electro-enzymatic activity. This allows the statistical distribution of biocatalytic activity across the population of decorated *fd*-particles to be resolved, as well as permitting the cross-correlation of the functional properties of the particles with their actual dimensions. Moreover, achieving sub-particle resolution enables to reveal a high activity region located in the middle of the particles, attributable to the interplay between charge transport, occurring via electron hopping between Fc moieties along the viral particles, and enzymatic catalysis. By quantifying and modelling such nanoscale 1D-reaction-diffusion coupling, full kinetic characterization of the *fd*-scaffolded integrated system is achieved, revealing differences in the functional behavior of the biocatalytic viral particles when addressed at the ensemble or at the single particle scale.

It is worth noting that SECM-derived techniques have recently been successfully used to image cellular biostructures a few 100 nm in size,[48,49] and also to interrogate inorganic catalytic nanoparticles at the ~10 nm resolution.[50–54] In this context of quickly expanding applications of nano-SECM,[55] our work provides the first demonstration of the ability of an electrochemical microscopy technique to probe the enzymatic activity of individual nano *bio*-objects at the single- and sub- particle scale.

Results and Discussion

Step by step assembly of a random array of Fc-PEG / PQQ-GDH immunodecorated *fd* on SiO_2.

The integrated Fc-PEG / PQQ-GDH system studied herein was assembled onto *fd*-bacteriophage particles acting as bio(nano)scaffolds.[25,47] *fd*-bacteriophage is a structurally well-defined and highly monodispersed, flexuous rod-like particle, 880 nm in length and 6.6 nm in diameter.[56] It is composed of ~2700 copies of a major coat protein, packed around a single-stranded circular DNA, and of a few copies of four other proteins forming its extremities. Key advantages of using this virus as the scaffold carrier include its structural robustness, ability to be produced at high yields, ease of handling, as well as its completely harmless nature to humans.[57]

fd-phage particles were adsorbed onto SiO_2 surfaces bearing a stable adhesion-promoting C11 amino-silane self-assembled monolayer (see methods section). Adsorption of the viral particles was carried out in a phosphate buffer pH 7.4 as, under these conditions, the negatively charged *fd*-particles adsorbed irreversibly onto the positively charged amino layer, forming random arrays (Figure S1). The surface was then protected against non-specific adsorption by a BSA backfilling step. The integrated system was subsequently assembled onto the *fd*-scaffolds using a step-by-step immunological process, which ensures both the *specific* immobilization of the molecular components of the system onto the *v*iral particles, and their correct orientation towards the bulk solution (Figure 1(*i*)). For this, the *fd*-bearing surface was sequentially exposed to solutions of: (i) rabbit anti-*fd*-capsid antibody (immunoglobulin G, IgG), (ii) GDH-anti-rabbit IgG conjugate, (iii) rabbit anti-GDH antibody and, finally, (iv) redox-labelled anti-rabbit IgG, bearing polyethylene glycol (PEG) chains terminated by a ferrocene group (Fc).[58] Experimental conditions for the assembly of the successive IgG layers were such that, at each assembly step, saturated layers of antibodies were formed on the scaffold. As demonstrated previously,[47] this ensured the growth of a well-defined hemi-cylindrical multilayered immuno-assembly on the *fd*-scaffolds, resulting in uniformly decorated particles (Figure S2).

In-situ Mt/AFM-SECM imaging of a random array of *fd*-particles decorated with the integrated Fc-PEG / PQQ-GDH system: Triggering and probing the catalytic activity of individual particles.

The SiO_2 surface bearing a random array of *fd*-particles decorated with the integrated system was imaged in-situ (in Tris buffer pH 7.5) by tapping mode Mt/AFM-SECM, making use of home-made gold probes (tips), able to act simultaneously as force sensors and ultramicroelectrodes.[59] The electrochemical tip potential was set to E_{tip} = +0.3 V/SCE, a value largely anodic with respect to the standard potential of the Fc heads of the PEG chains ($E°$ = +0.15 V/SCE).

Simultaneous topography and current Mt/AFM-SECM images of the surface, acquired in the absence of glucose - the enzymatic substrate of GDH- are reproduced in Figure 1B(*i*),

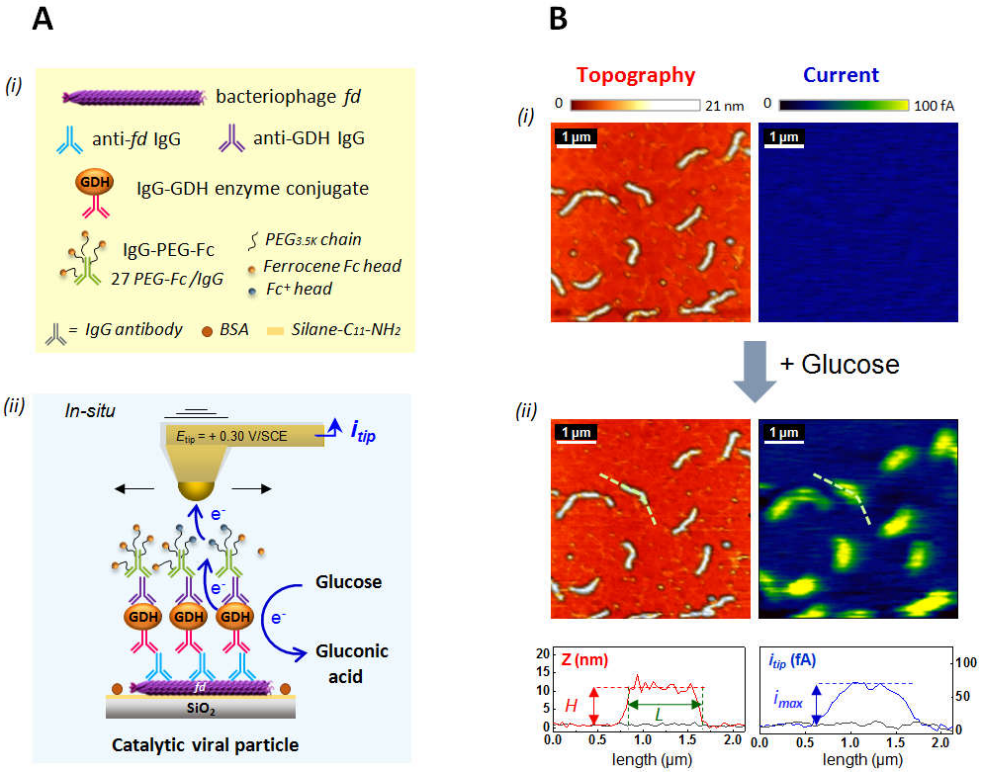

Figure 1. (A) Molecular components of the Fc-PEG / PQQ-GDH integrated system immuno-assembled onto *fd*-particles, (*i*), functional interrogation of the resulting scaffolded integrated system by a Mt/AFM-SECM tip (*ii*). (B) In-situ tapping-mode Mt/AFM-SECM imaging of a random array of Fc-PEG / PQQ-GDH immunodecorated *fd*-particles adsorbed on a SiO_2 surface. Shown are the simultaneous topography and tip current images of the very same particles, acquired in the absence (*i*) and after the addition (*ii*) of 10 mM glucose. Tip potential E_{tip} = + 0.3 V/SCE. Imaging buffer: Tris buffer pH 7.5. The correlated height and current profiles shown in (B) are image cross-sections taken along the dotted line.

Individual and well-defined decorated *fd*-particles can be clearly identified in the topography images, as elongated objects. It can also be seen that, at the opposite, no object whatsoever appear in the simultaneous current image. The tip was then withdrawn a few microns above the surface and glucose was injected into the cell, up to a concentration of 10 mM. The tip was then brought back into contact with the sample surface and the surface reimaged. As can be observed from the topography image presented in Figure 1B(*ii*) the very same particles imaged before glucose injection can then be recognized from their particular shape, and from the patterns they form. Strikingly, these particles that were undetected in the initial current image, in the absence of glucose, now appear as bright elongated spots after glucose injection.

The clear spatial correlation between the tip current and topography images recorded in the presence of glucose, and the total absence of current between the particles, demonstrates that the tip current is specifically generated by the Fc-PEG / PQQ-GDH integrated system borne by the *fd*-particles, (Figure 1A(*ii*)). Upon interacting with a decorated *fd*-particle, the appropriately biased tip oxidizes the PEG-attached Fc heads into their Fc^+ form which, as shown previously, acts as a very efficient redox cosubstrate for the PQQ-GDH catalyzed oxidation of glucose.[47] As a result of this enzymatic reaction, the reduced Fc form of the mediator is generated and fed back to the tip to be further oxidized. Hence, the tip *triggers* the enzymatic redox cycle that, in turn, generates a stationary tip current reflecting the local catalytic activity of the individual particle interrogated. The Fc-head-mediated nature of the enzymatic process was confirmed by the fact that the intensity of the current spots was shown to vary with the tip potential following a typical S-shaped curve centered around a value of 0.14 V/SCE, i.e. close to the standard potential of the Fc heads, E_o = 0.15 V/SCE (Figure S4). No current was detected when the tip was biased at potentials such that $E_{tip} << E_o$, where no Fc^+ was generated, while for $E_{tip} >> E_o$ the current became E_{tip} independent, indicating infinitely fast Fc^+ generation at the tip. It is worth noting that, when the Fc-PEGylated IgG was omitted from the construction, no current spots were recorded, evidencing that the observed biocatalysis takes place via the Fc-PEG serving as the sole cosubtrate present for GDH.

It is worth pointing out that absolutely *all* of the hundreds of decorated *fd*-particles we imaged throughout this study were associated with a current spot, illustrating the high efficiency of the immunoassembly process employed to construct the integrated system on the *fd*-scaffolds. However, examining the current image shown in Figure 1B(*ii*), one can see that the spots associated with the viral particles vary in intensity, evidencing a distribution of catalytic activity across the decorated particles population. Owing to its single particle resolution, Mt/AFM-SECM enables quantitative study of this intrinsic statistical property of nano-scaffolded enzymatic systems.

Quantifying the statistical dispersion of the catalytic and topographic properties of decorated *fd*-particles, and exploring their cross-correlations.

Examination of height profiles taken along the contour of particles visible in the topography image enables the measurement of their apparent dimensions (red trace plot in Figure 1B(*ii*)). The particle contour length, L, and the particle height averaged along the particle contour, H, were chosen as the topographic parameters of interest. The particle width was not considered as meaningful here as, in AFM, the width of objects is overestimated due to tip convolution effects, to an extent that depends on the relative sizes of the imaged object and the imaging tip. This effect is expected here to be (and is) more pronounced for current than for topography images (see SI). For consistency, the data reported in the present paper were thus acquired with a limited set of tips, having a similar radius of ~100 nm.

The catalytic activity of *individual* particles can be quantified by taking particle profiles in the current images, following the contour paths defined from the topography image (blue trace plot in Figure 1B(*ii*)). One then measures the value of the parameter i_{max}, defined as the maximum intensity of the catalytic current recorded for any given particle.

The statistical distribution of the catalytic and topographic properties across the decorated *fd*-population can be analyzed by constructing i_{max}, L and H histograms, Figure 2.

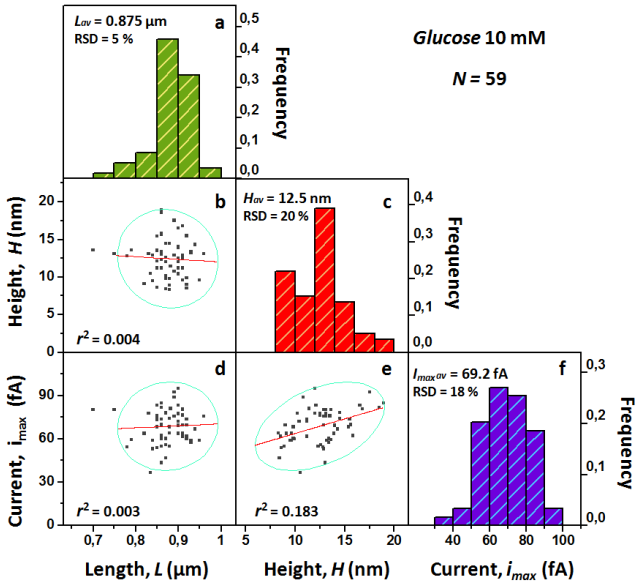

Figure 2. Statistical distribution of the geometric and catalytic properties of Fc-PEG/ PQQ-GDH decorated *fd*-scaffolds as reflected by histograms of their: (a) length, *L*; (c) height, *H*; (f) characteristic catalytic tip current intensity, i_{max}. Data were acquired from the analysis of Mt/AFM-SECM images of $N = 59$ individual decorated *fd*-particles. Medium: Tris Buffer pH 7.5 containing 10 mM glucose. Tip potential $E_{tip} = +0.3$ V/SCE. (b), (d) and (e) are cross-correlations plots, where two of the characteristic parameters (*L, H* or i_{max}) measured for each of the particles are plotted as a function of one another: (b) and (d) show the *L* dependence of *H* and i_{max}, respectively, (e) shows the dependence of i_{max} on *H.* The red lines in (b), (d) and (e) are linear regression lines, the corresponding squared Pearson's correlation coefficients (r^2) are shown.

The particle length histogram, Figure 2a, shows that the length of the decorated *fd*-particles is narrowly distributed (relative standard distribution, RSD of 5 %) around an average value of $L_{av} = 875$ nm, which closely matches the nominal length of the bare *fd*-particle itself (880 nm). In Figure 2c, it can be observed that the height of the decorated particles is somewhat more broadly distributed (RSD = 20 %), around a statistical average value of $H_{av} = 12.5$ nm. This value is substantially lower than the estimated decorated particle height of ~80 nm, as calculated from the nominal dimensions of the macromolecules constituting the integrated system. This result indicates that the multilayered antibody assembly on the virus is too soft and flexible to be sensitively detected in topography by AFM-tips (see Figure S2 and associated discussion in SI).[60]

Of particular interest is the catalytic tip current, i_{max}, histogram presented in Figure 2f, as it uniquely enables one to visualize and quantify the statistical distribution of the electro-enzymatic activity of the decorated *fd*-particles. It can be seen from this plot that the activity of the particles follows a relatively

symmetrical distribution around an average catalytic current value of ~70 fA per particle, and is characterized by an RSD value of ~18%. This value is significantly higher than the 5% error margin that characterizes the reproducibility of our tip current measurements.

Interestingly, the average catalytic tip current is close to the characteristic current of 100 fA per *fd*-particle, which we determined previously from ensemble CV measurements, carried out on the very same *fd*-scaffolded Fc-PEG/IgG-GDH integrated system displayed on gold electrodes.[47] This result is most intriguing as one would expect that the tip current, which results from the activity of *a limited* number of GDH molecules located below the tip, would be much lower than the current per particle value measured by CV, which corresponds to the activity of *all* of the GDH molecules borne by each particle. The fact that both techniques yield comparable current per particle values implies that the tip can apparently address a much larger number of GDH molecules than mere physical contact between the tip and the decorated *fd*-particles could a priori allow. Indeed, the interaction area of the ~100 nm radius tip with the decorated *fd* is expected to encompass only a small fraction of the full virus length, for mere geometric reasons (Figure S7).

A likely mechanism by which the tip could collect electrons from remotely located GDH molecules is Fc^+ propagation along the *fd* capsids. This is made possible by the complex and composite nature of the processes generating the electrocatalytic current (Figure 3A): Upon touching the Mt/AFM-SECM tip, the PEG-borne Fc heads are locally oxidized into their Fc^+ form. The elasticity of the PEG chain enables Brownian elastic motion of the Fc^+ heads over ~10 nm, a distance small enough to favor the encounter and electron exchange with neighboring Fc heads. Such a combined elastic diffusion / electron hopping mechanism enables the Fc^+ heads to propagate *along* the *fd* capsid, until they are consumed by the enzymatic reaction, and converted back to their Fc form. The efficiency of this charge transport mechanism for conveying Fc^+ across hundreds of nanometers within antibody assemblies, and toward the catalytic site of redox enzymes, has been demonstrated in our earlier works.[61] More generally electron hopping between surface-confined Fc moieties, forming monolayers,[62,63] or entrapped within thin films, has been extensively described in literature.[64]

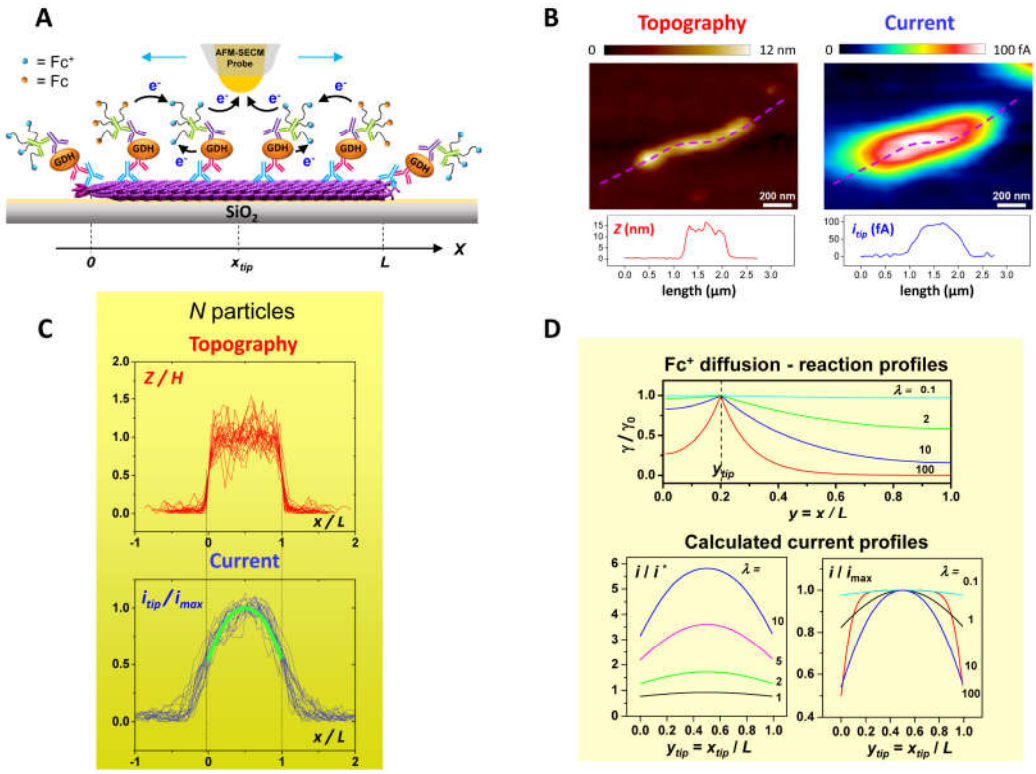

Figure 3. (A) Schematics of the processes associated with the electrochemical interrogation of the Fc-PEG/ PQQ-GDH decorated *fd*-particles by Mt/AFM-SECM: Fc^+ generation at the tip, electron transport along the *fd*-particle between neighboring Fc/Fc^+ heads, and enzymatic catalysis (glucose is omitted for clarity). (B) High-resolution tapping mode Mt/AFM-SECM images of an individual Fc-PEG/ PQQ-GDH decorated *fd*-particle. Simultaneously acquired topography and tip current images are shown together with the profiles taken along the dotted line as drawn. (C) Normalized topography (upper graph) and tip current (lower graph) profiles, taken along the long axis of 25 decorated *fd*-particles and superimposed. The green line in the current profiles plot is a theoretical profile calculated using Equation 5 with $\lambda = 10$. (D) Top:.theoretical Fc^+ concentration profile along a *fd*-particle, calculated with Equation (2). Bottom: dimensionless theoretical current profiles calculated using Equation 3 (left plot) or Equation 5 (right plot). Plots were calculated with the values of λ indicated.

In order to gain insights into the coupling between such Fc^+ propagation and enzymatic activity on *fd*-particles, the possible relationships between the particle dimensions and activity was explored. This is made possible by the fact that Mt/AFM-SECM is a *correlative* imaging technique enabling the values of the three parameters i_{max}, L, and H to be measured for each individual decorated *fd*-particle imaged.

It was thus possible to construct cross-correlations plots, where the value of i_{max}, measured for each of the particles interrogated was plotted as a function of either the length L or the height H of the very same particle (Figures 2d and 2e respectively). The i_{max} vs. L plot (Figure 2d) does not evidence any

obvious correlation between the particle length and catalytic activity. At the opposite the i_{max} vs. H plot (Figure 2e) reveals that the particle activity is moderately correlated to the particle height.

Probing the catalytic activity of individual decorated *fd*-particles. Analysis of the topography and current profiles taken along the particles.

To further investigate the relationship between the catalytic activity of the decorated *fd*-particles and their dimensions, we closely examined high-resolution current and topography images of individual decorated *fd*-particles. As exemplified in Figure 3B, we observed that a region of maximum catalytic tip current intensity was typically located near the *center* of the *fd*-particles (also see Figure S8). To quantify this intriguing observation, we took current and height profiles along the contour of a series of 25 particles. The resulting superimposed sets of topography and current profiles are displayed in Figure 3C, upper and lower plots respectively. In order to take into account the statistical distribution of the particle length, the abscissa, x, of each individual profile was normalized by the actual length, L, of the corresponding particle. Similarly, the ordinate of the individual topography, Z, and current, i_{tip}, profiles were normalized by the values of H and i_{max} derived for each *fd*-particle. The resulting normalized topography and current profile plots enabled several general trends to be identified.

One can see that the general shape of the topography profile is seemingly rectangular, displaying a "rough" top region extending over almost the full length of the viral particle (x/L = 0 to 1). The actual 1-2 nm 'roughness' of this plateau region probably reflects the "grainy" nature of the assembly, which consists of discrete macromolecular entities (IgGs, GDH and Fc-PEG chains) imperfectly sensed by the tip. The sharp rise and fall of the topography profile on each side of the "plateau" is also coherent with the scenario outlined above of the tip mostly interacting with the robust *fd* capsid (and only weakly with the IgGs). The same is valid to explain the close match between the average L and nominal (bare) *fd*-particle length values.

Unlike the topography profiles, the superimposed set of tip current profiles (Figure 3C) does not display any plateau region, but is actually bell-shaped. This is intriguing as it means that the tip current

actually varies continuously in the region spanning from x/L = 0 up to x/L=1, where the tip is actually positioned above the capsid of the particle, passing through a maximum located at the particle mid-length. As a result, an apparent *catalytic "hot-spot"* appears along the middle of the decorated *fd*-particles (Figure 3B and Figure S8).

One can also notice in Figure 3C that the tip current slightly extends beyond the region spanning from x/L = 0 up to x/L=1. This can be explained by the tip making contact with the part of the immunoassembly that "overhangs" each end of the *fd*-particle, before "touching" the viral particle itself (Figure 3A). This tip-convolution effect can be quantitatively reproduced by considering the dimensions of the *fd*-supported immunoassembly and the tip radius, as detailed in supporting information (Figure S6 and Figure S7).

In order to rationalize all of our above observations, notably regarding the intensity and spatial distribution of the catalytic tip current over the *fd*-particles, we developed a mathematical model describing Fc^+ transport along the *fd*-particle coupled to enzymatic catalysis, as follows.

Modelling the tip-triggered enzymatic catalysis taking place on individual decorated *fd*-scaffolds.

In order to reduce the number of parameters involved in modeling the enzymatic electrocatalysis, locally triggered (and probed) by the AFM-SECM tip, we considered the decorated *fd*-particles as homogenous 1D objects, of length L. The high aspect ratio of the *fd*-scaffold makes this simplifying assumption reasonable. Besides, we verified that the tip catalytic current did not depend on the actual curvature of the decorated *fd*-particles (Figure S5). Considering the 1D dimension of the model, the tip is viewed as a single point, located on the virus at a position x_{tip} (Figure 3A), from which Fc^+ can propagate toward each of the virus extremities.

We modeled Fc^+ propagation along the viral capsid as an effective diffusional process, as is typical (albeit approximate) for charge transport by electron hopping between redox sites.[65] We thus introduced an effective "electron" diffusion coefficient, D_e. The reaction of PQQ-GDH with the Fc^+ co-substrate

was, as a first approach, modeled as a first order reaction, characterized by a first order rate constant, k_{app} (the validity of this assumption is discussed in details below).

The model thus assumes that the decorated *fd*-particle behaves as a continuous medium, displaying homogeneous electron transport and enzymatic properties. This assumption is justified by the high homogeneity of the antibody coverage of the *fd*-scaffold evidenced by high resolution AFM images (Figure S3), as discussed above.

Hence, Fick's law can be used to describe the space dependence of the *linear* Fc^+ concentration, γ, all along the virus capsid. The 1D Fick's equation to be considered is then:

$$D_e \frac{\partial^2 \gamma}{\partial x^2} - k_{app}\, \gamma = 0 \qquad (1)$$

This equation can be solved by taking into account the following boundary conditions:

(i) At each viral particle extremity ($x = 0$ and $x = L$), the Fc^+ flux is zero:

$$\frac{\partial \gamma}{\partial x} = 0$$

(ii) At the tip electrode surface, $x = x_{tip}$: The tip being biased at a potential $E_{tip} >> E°_{Fc}$, the Fc heads can only exist in their Fc^+ form, so that $\gamma = \gamma_0$, where γ_0 is the total linear ferrocene heads concentration borne by the virus (in number of Fc heads per unit length).

By resolving Equation 1 the following analytical expression is obtained. It gives the concentration profile of Fc^+ along the *fd*-particle, for any position of the tip on the virus, x_{tip}:

$$\gamma = \gamma_0 \{ cosh(\sqrt{\lambda}[1 - y]) / cosh(\sqrt{\lambda}[1 - y_{tip}]) \} \qquad (2)$$

where $y_{tip} = x_{tip}/L$ and $y = x/L$ are the dimensionless tip position and coordinate along the virus, respectively.

The profile depends on a single dimensionless kinetic parameter, $\lambda = k_{app} L^2 / D_e$, which compares the rate of catalysis to the rate of diffusion along the full length of the virus.

A few Fc^+ concentration profiles, calculated for a few λ values, and for a tip positioned near one extremity of the decorated *fd*-particle (x_{tip}/L= 0.2) are plotted in Figure 3D. One can observe that the

stationary Fc^+ concentration profile developing on each side of the electrode extends along the virus capsid, over a typical length of ~$1/\sqrt{\lambda}$. Depending both on the tip position and on the λ value, the concentration profiles can reach both the nearest or eventually none of the virus extremities. In any case, the tip actually addresses GDH molecules remotely located on the virus capsid, "via" the Fc^+ profile. This justifies the above discussed experimental observation of a tip current generated by more enzyme molecules than those located immediately above the tip.

The expression of the catalytic tip current value, i_{tip}, is given by the first derivative of the Fc^+ profile:

$$i_{tip} = i^*\sqrt{\lambda}\{tanh(\sqrt{\lambda}y_{tip}) + tanh(\sqrt{\lambda}[1 - y_{tip}])\} \quad (3)$$

where $i^* = FD_e\gamma_0/L$, is a characteristic (non-catalytic) tip current.

The variation of the normalized catalytic tip current (i_{tip}/i^*) with the tip position, calculated for various values of λ, is illustrated in Figure 3D. One can see that the magnitude of the theoretical tip current profiles depends sharply on the λ value: the higher the enzymatic activity as compared to the Fc^+ diffusion rate, the higher the expected current. However, one also sees that, no matter the λ value, the current always reaches its maximum intensity *at the center of* the *fd*-particle. This maximal theoretical current value, obtained from Equation 3 with $y_{tip} = 0.5$ is given by:

$$i_{max} = 2i^*\sqrt{\lambda}\,tanh(\sqrt{\lambda}/2) \quad (4)$$

Normalizing i_{tip} by i_{max} shows that the actual *curvature* of the tip current profile solely depends on the exact λ value (Figure 3D, lower right plot).

$$i_{tip}/i_{max} = \{tanh(\sqrt{\lambda}y_{tip}) + tanh(\sqrt{\lambda}[1 - y_{tip}])\}/\{2\,tanh(\sqrt{\lambda}/2)\} \quad (5)$$

Two interesting limiting situations are reached for extreme values of λ:

∗ λ >>1: $i_{max} = 2FD\gamma_0\sqrt{k_{app}D_{eff}}$, this situation corresponds to the enzymatic rate being much higher than the F_C^+ propagation rate, and is characterized by a tip current becoming independent of the virus length, *L*. In that situation the F_C^+ diffusion layer only reaches the extremity of the *fd*-particles when the tip is very close to the extremity.

* $\lambda \ll 1$: $i_{max} = F\gamma_0 k_{app} L$, this situation corresponds to the enzymatic rate being much slower than the Fc^+ propagation rate, and is characterized by a tip current becoming proportional to virus length, L. In that case the Fc^+ diffusion layer encompasses the whole particle length.

Thus, we have so far demonstrated, on the basis of a simple model that the combination of Fc^+ transport and its enzymatic consumption can fully account for the apparent "catalytic hot-spot", appearing at the *central* region of the viral particles. Besides, the apparent lack of dependence of the catalytic tip current on the virus length observed in Figure 2d can be justified by a high λ value situation.

Importantly the mere fact that bell-shaped catalytic profiles were experimentally observed confirms that the IgG-PEG-Fc and the IgG-GDH antibodies were homogenously distributed along the *fd*-particles. Indeed, inhomogeneous decoration by these antibodies would result in local variation of the electron hopping rate and/or enzymatic activity along the viral particles, i.e. in zones of non-uniform catalytic activity. Depending on their extent, these zones would modulate the tip current in a detectable way, resulting in non-bell shaped current profiles. We demonstrated the possibility of mapping such local variations in catalysis by imaging (rare) fragmented decorated *fd*-particles that, unlike intact particles, were found to display marked high and low activity zones (see Figure S10).

Our model suggests that, in any case, the *curvature* of the central region of S-shaped tip current profile, observed for all intact decorated *fd*-particles, can be used to access the value of the kinetic parameter λ, without having any a priori knowledge of the individual values of the parameters involved (k_{app}, D_e,…).

We therefore fitted Equation 5 to the overlapped experimental catalytic tip current profiles shown in Figure 3C, using λ as a sole adjustable parameter, and determined a best fit value of $\lambda \sim 10$, (thick green trace). Reporting this λ value, together with the average i_{max} value of 70 fA determined above, into Equation 4, it yields: $i^* = FD_e\gamma_0/L \sim 12$ fA. Since we previously measured that the average number of Fc heads borne by the decorated *fd*-particles was about $n_{Fc} \sim 4000$, and taking L = 880 nm, one can

estimate a γ_0 value of $\gamma_0 = n_{Fc}/L = 4.5$ Fc per nm. Hence, from the above given expression of i^* we obtain: D_e = 1.5 10^{-7} cm^2/s. This value is larger than the physical diffusion coefficient of the PEG-attached Fc heads, that we previously estimated ((2 - 5) 10^{-8} cm^2/s),[66,67] indicating the effective contribution of electron hopping to the Fc^+ propagation. This result evidences that confinement of the flexible Fc-PEG chains on the *fd*-scaffold enables a fast electron transport rate, which, as shown previously, contributes to enhance the catalytic performance of the Fc-PEG/GDH integrated system, as compared to non-scaffolded systems.[47] The question that arises now is how can one quantitatively characterize the full kinetic behavior of individual decorated *fd*-particles from Mt/AFM-SECM measurements using our model?

This requires that the dependence of the catalytic activity of the decorated *fd*-particles on glucose concentration is studied.

Dependence of the catalytic activity of individual decorated *fd*-particles on glucose concentration.

Thanks to the nondestructive character of tapping mode Mt/AFM-SECM, together with its high spatial resolution and stability, we were able to image decorated virus particles repeatedly while injecting increasing amounts of the enzymatic substrate glucose in solution. Figure 4A shows the correlated current and topography images of several particles, recorded for various glucose concentrations in the 0-100 mM range.

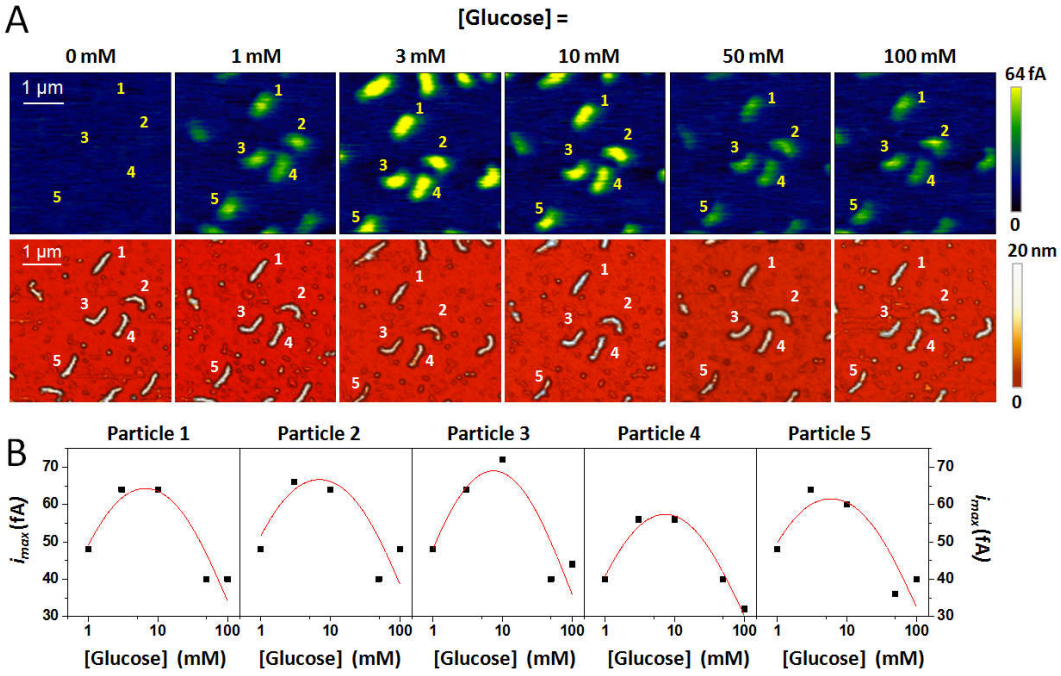

Figure 4. (A) Mt/AFM-SECM images of individual Fc-PEG/ PQQ-GDH decorated *fd*-particles recorded at various glucose concentrations (indicated on top of the images). The very same particles were imaged recursively after incremental injections of glucose. Five particles, labelled 1 to 5, appear in their entirety in all of the images. (B) Kinetic plots showing the variation of the catalytic tip current, i_{max}, as a function of glucose concentration for each of the 5 indexed particles. The red curves are guides to the eye. Tip potential E_{tip} = + 0.3 V/SCE. Imaging buffer: Tris buffer pH 7.5

It can be observed that, in spite of a slight drift of the images, five particles (indexed from 1 to 5) appear in their entirety in each of topography and current images recorded at each of the glucose concentrations explored. Interestingly, examination of the sequence of current images also shows that the intensity of the current spots associated with the particles first increases when glucose is injected, up to ~ 10 mM, and then decreases upon extra-injections of glucose. This trend is attributed to the known reversible inhibition of the PQQ-GDH enzyme by its substrate.[68] This behavior can be quantified by plotting the variation of the catalytic tip current, i_{max}, with the glucose concentration, for all of the particles interrogated, (Figure 4B).

Being able to plot such kinetic curves yields an unprecedented access to the kinetic behavior of *individual* enzymatically decorated scaffolds. This uniquely enables us to address the issue of the statistical dispersion of the *kinetic behavior* of the biocatalytic *fd*-particles across their population, and to track down its origin.

Examination of the kinetic plots reproduced in Figure 4B reveals that, for all of the particles interrogated, qualitatively similar bell-shaped variations of the catalytic tip current with glucose concentration are obtained. Yet, one also notices that the magnitude of the curves can differ from one particle to the other, and so can possibly the exact shape of the curves (Figure 4B). In order to reveal the similarity and differences of kinetic curves recorded for different particles, we constructed the cross-correlation plots, where the catalytic tip current, i_{max}, recorded for any given particle at every glucose concentration explored, is plotted versus the i_{max} values measured for all of the other particles (Figure 5A).

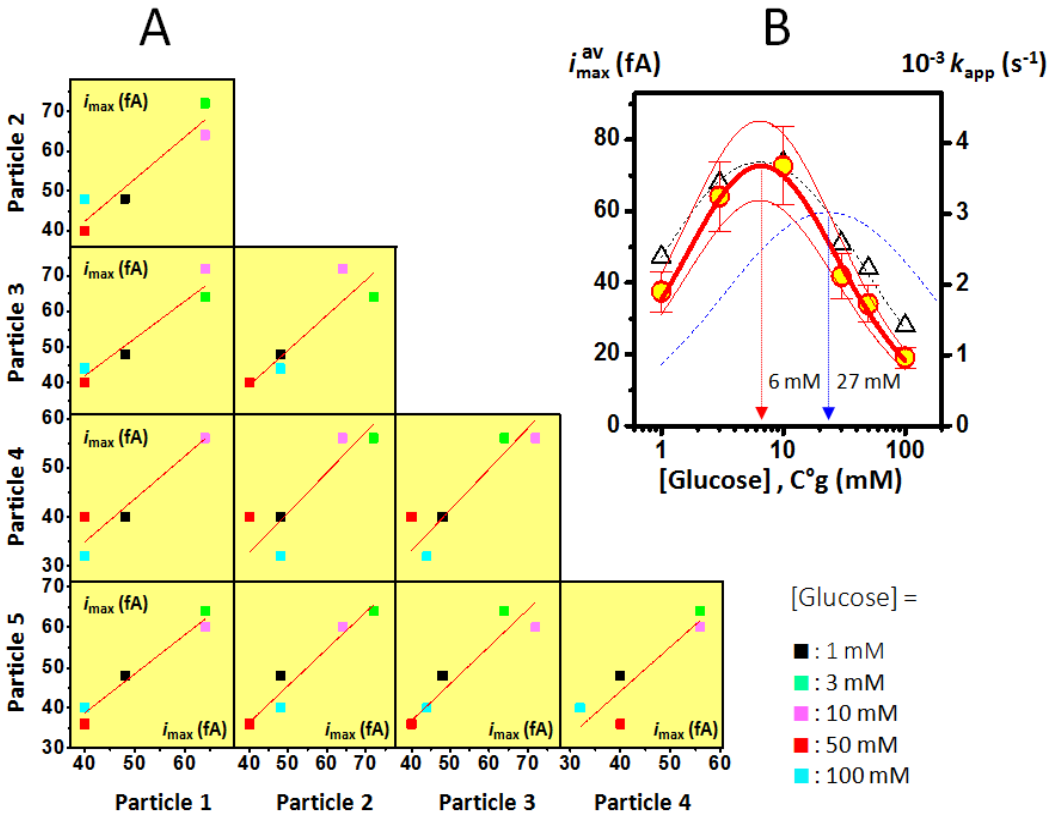

Figure 5. (A) Cross-correlation plots where the catalytic tip currents i_{max} (fA) corresponding to the particles labelled [1, 2, 3, 4 and 5] in Figure 4, and recorded at every glucose concentration explored, are plotted as a function of each other. Red traces are least square regression lines passing through the origin. (B) Kinetic plots characterizing the catalytic glucose oxidation by the *fd*-supported Fc-PEG/PQQ-GDH integrated system. Triangles: Variation of the *particle-averaged* experimental catalytic tip, i^{av}_{max} current with the glucose concentration. The black dashed line is a guide to the eye. Yellow dots: Calculated apparent first order catalytic rate constants, k_{app}, as derived from i^{av}_{max} values using Equations 4 and 8. Red curves: Best fits of the kinetic Equation 9 to the experimental k_{app} vs. C°g data, either considering the central values (thick line) or boundary values corresponding to a ±15 % error margin (thin lines). Dotted blue curve: Dependence of the experimental k_{app} value measured at the ensemble scale by cyclic voltammetry in our previous work.[47]

One can clearly visualize that the data points presented in all of the cross-correlation plots tend to align along straight lines passing through the origin. This result indicates that the catalytic tip current determined for all of the particles are simply proportional to each other. To interpret this result on a kinetic basis, it is interesting to recall that the rate law for the oxidation of glucose, catalyzed by surface immobilized GDH, using Fc^+ as a redox cosubstrate, can be written under the following general form, valid both for its slow (noncooperative) or fast (cooperative) kinetic modes:[69]

$$v_{ez} \propto n_E \Big/ \left[\frac{1}{k_{ox}\,[Fc^+]}\left(1 + K_i C_g^0\right) + \frac{1}{k_{cat}} + \frac{K_M}{k_{cat} C_g^0}\right] \qquad (6)$$

where v_{ez} is the enzymatic rate, n_E is the number of GDH molecules involved, [Fc^+] the "local" Fc^+ concentration as "seen" by the enzyme, $C°g$ the bulk glucose concentration. k_{cat} is the catalytic constant of the enzyme, K_M the Michaelis constant for glucose, k_{ox} the second-order rate constant corresponding to the oxidation of the enzyme by Fc^+, and K_i the equilibrium constant of the enzyme inhibition by glucose.

From Equation 6, it can be deduced that the proportionality between the catalytic current for different *fd*-particles, over the whole range of the glucose concentrations, implies that the particles only differ by the number of GDH enzyme they bear, n_E. Indeed, had they individually followed rate laws differing by their dependence on glucose concentration, or even had the values of the GDH kinetic constants differed from one particle to the other, no such linear correlation would have been obtained. This result demonstrates that the microenvironment provided to the GDH enzyme by the *fd*-scaffolds is extremely homogeneous across the *fd* population, and as a result all of the particles display identical kinetic behaviors. Hence, one can conclude that the distribution in catalytic tip current quantified above simply represents the particle-to-particle variation in the amount of GDH molecules they bear, thus characterized by a relative standard dispersion of 18 %. This relatively narrow distribution is a benefit of the high yield of the immunological assembly technique used to decorate the *fd*-scaffolds, rooted in the very high affinity of the polyclonal antibodies for their macromolecular antigens. Indeed, as

previously determined,[47] the average number of GDH molecules per *fd* is n_E^{av} = 230 ± 30, and corresponds to a saturating coverage of the virus capsid.

A welcome consequence of the uniform kinetic behavior of the biocatalytic *fd*-particles is that it makes averaging of the kinetic curves recorded for multiple particles legitimate. This yields a unique representative particle-averaged tip current, i_{max}^{av}, versus C°g plot (Figure 5B), whose well-defined bell-shaped variation is, as stated above, typical of the kinetic behavior of PQQ-GDH with respect to glucose. Also shown in Figure 5B, is the corresponding (normalized) kinetic curve we reported previously for the *fd*-decorated particles probed at the ensemble scale by CV. It is noticeable that the i_{max}^{av} vs. C°g curve derived from single *fd*-particle measurements is significantly shifted toward lower glucose concentrations as compared to the kinetic plot corresponding to the ensemble scale measurement. The glucose concentrations corresponding to the peak of the i_{max}^{av} vs. C°g variations obtained for the single particle and ensemble measurements are 6 ± 1 mM and 27 ± 3 mM, respectively. Revealing the cause of this scale-effect on catalysis requires that the kinetic parameters of the *fd*-supported Fc-PEG / PQQ-GDH system are carefully extracted from the Mt/AFM-SECM data.

Analyzing the kinetics of GDH action at the single *fd*-scaffold scale.

The i_{max}^{av} vs. C°g curve contains the sought information regarding the kinetic behavior of *fd*-supported GDH, but its quantitative interpretation requires that an actual enzymatic turnover rate is obtained from the i_{max}^{av} values. This imposes that Equation 1, ultimately enabling to calculate i_{max}, is modified to incorporate the full kinetic expression characterizing PQQ-GDH-catalyzed oxidation of glucose, given by Equation 6. The modified equation is:

$$D_e \frac{\partial^2 \gamma}{\partial x^2} - \frac{2k_{ox}\gamma_E \gamma}{(1+K_i c_g^0)+\gamma\left[\frac{k_{ox}}{k_{cat}}\left(1+\frac{K_M}{k_{cat}c_g^0}\right)\right]} = 0 \qquad (7)$$

where $\gamma_E = n_E^{av}/L$, is the linear enzyme concentration on the *fd*-particle.

This non-linear differential equation can be solved numerically on the basis of two dimensionless kinetic parameters $\lambda^* = 2k_{ox}L^2\gamma_E/\left[D_e\left(1+K_iC_g^0\right)\right]$ and $\sigma = k_{ox}\gamma_0\left(1+K_M/C_g^0\right)/\left[k_{cat}\left(1+K_iC_g^0\right)\right]$ (see supporting information).

A simplification is however possible, realizing that in the practical range of λ = 1...30 and σ = 0...10, Equation 7 yields i_{max}/i^* values which are numerically similar (within 20%) to those derived with Equation 1 using an "equivalent" λ value of $\lambda = \lambda^*/(1+\sigma)$. This simplification allows us to use the analytical expression (4), together with the above-determined i^* = 12 fA value, to convert experimental i_{max} values into λ values.

Finally, a first order catalytic constant (apparent turnover), k_{app}, characterizing the overall enzymatic rate, can then be derived from the experimental λ values as:

$$k_{app} = \lambda \times D_e\gamma_0/L^2\gamma_E \qquad (8)$$

k_{app} is related to the full expression of the enzymatic rate law as:

$$k_{app} = 2k_{ox}\gamma_0/\left[\left(1+K_iC_g^0\right)+k_{ox}\gamma_0\left(1+K_M/C_g^0\right)/k_{cat}\right] \qquad (9)$$

Variation of the experimental value of k_{app} with the glucose concentration is plotted in Figure 5B, yellow filled symbols. Equation 9 was used to fit the data points, allowing the experimental bell-shaped variation to be very satisfyingly reproduced (thick red line), and yielding the set of best-fit kinetic parameters reported in Column (I) of Table 1.

	(I)	(II)	(III)	(IV)
Enzymatic constants	***fd*-scaffolded system Mt/AFM-SECM (Single particle scale)**	***fd*-scaffolded system CV (Ensemble scale)**	**GDH in solution Fc in solution *Non-coop. mode***	**GDH in solution Fc in solution *Coop. mode***
k_{cat} (s^{-1})	10000 ± 4000	8500 ± 1500	1500 ± 300	6000 ± 1000
K_M (mM)	8 ± 3	14 ± 2	0.27 ± 0.005	4.7 ± 0.3
K_i (M^{-1})	90 ± 35	11 ± 3	52 ± 6	127 ± 20
$k_{ox}\, C_p^E$ (s^{-1})	N.A.	3000 ± 700	N.A.	N.A.
$k_{ox}\, \gamma_0$ (s^{-1})	5000 ± 2000	N.A	N.A.	N.A.

Table 1. Sets of kinetic constants, characterizing the catalytic activity of PQQ-GDH in various systems, configurations and kinetic modes as indicated. Columns (I) to (II) (gray background) present data for the *f*d-scaffolded Fc-PEG/PQQ-GDH system, derived either from single particle Mt/AFM-SECM experiments (this work), or ensemble scale CV studies (reference [47]), respectively. Columns (III) and (IV) present data from reference [69]. N.A. = non-applicable.

The K_i, k_{cat} and K_M values, characterizing the enzymatic action on glucose, can be directly compared to those reported for PQQ-GDH acting in solution, both in its non-cooperative and cooperative kinetic modes, which are reproduced in Table 1, Columns (III) and (IV), respectively.[69]

We observe that the K_i, k_{cat} and K_M values derived here are close to those typical of the cooperative mode of PQQ-GDH. This result is in agreement with our previous finding that confinement of the integrated system on the *fd*-scaffold turns the enzyme into its fastest kinetic mode.[47] Moreover, it also demonstrates the validity of our Mt/AFM-SECM approach, and its associated theoretical model, for probing and analyzing the catalytic activity of individual nano-scaffolded integrated enzymatic systems.

Also of interest is to compare the set of K_i, k_{cat} and K_M values we determined by our single particle approach, to those derived from our previous ensemble scale CV measurements, presented in Table 1 Column (II).[47] We find a good agreement between the k_{cat} and K_M values derived for the *fd*-scaffolded system from either CV or Mt/AFM-SECM experiments. However, the K_i value measured at the single particle level is ~9 times higher than the corresponding value measured at the ensemble scale. Such a large difference in K_i explains the dissimilar peak positions of the i_{max}^{av} vs. C°g kinetic plots obtained

from CV or Mt/AFM-SECM measurements (Figure 5B). This result suggests that the inhibition of PQQ-GDH by glucose is less intense when the system is probed at the ensemble scale, than at the single particle scale. The similarity between the K_i value derived by Mt/AFM-SECM, and the one reported for the enzyme in solution, points to an artificially low level of inhibition in ensemble scale CV experiments being the cause of this unexpected measurement scale effect. This may be due to the fact that, in CV, *all* of the decorated *fd*-particles borne by the electrode are triggered simultaneously, potentially leading to some degree of glucose depletion near the electrode surface, and consequently to lower inhibition. However, this is not an issue in Mt/AFM-SECM, where only a single *fd*-particle, specifically addressed by the tip, is catalytically functioning.

The $k_{ox}\gamma_0$ kinetic parameter we determined herein represents the net rate of oxidation of PQQ-GDH by the Fc^+ heads. It can be compared to the equivalent parameter obtained from our previous CV studies, originally labeled $k_{ox}\ C_p^E$, where C_p^E was the volume concentration in Fc^+ seen by the enzyme, and reported in Column (II) of Table 1.[47] One can see that the values derived for these parameters, either by studying individual particle kinetics, or at the ensemble scale, are similar. Such a result further underlines the self-coherence of our multi-scale quantitative analysis of the catalytic activity of the *fd*-scaffolded Fc-PEG/PQQ-GDH integrated system.

Conclusion

We have shown herein that Mt/AFM-SECM can be used as a powerful single particle correlative microscopy technique to resolve the position, acquire the topography and simultaneously probe the catalytic activity of individual viral nano-bioscaffolds bearing integrated enzymatic systems. This not only enables sampling of the statistical distribution of the topographic and catalytic activity parameters across the bioscaffold population, but also to investigate meaningful cross-correlations between them.

Beyond that, we also demonstrated that the sub-particle resolution achievable by Mt/AFM-SECM allows the enzymatic activity of individual viruses to be spatially mapped.

More specifically, in the present case of the *fd*-bacteriophage scaffolded Fc-PEG/PQQ-GDH system, the high-resolution allowed the presence of a high activity region located along the centre of the filamentous *fd*-scaffold to be revealed. Quantitative modelling enabled identification of electron hopping-based propagation of the active form of the enzyme co-substrate along the viral nanoscaffolds, and its coupling with the enzymatic reaction to be the source of this unexpected catalytic hot-spot. The model developed then enabled the catalytic tip current to be converted into meaningful kinetic data, which in turn permitted the unprecedented, complete, analysis of the GDH kinetics at the single *fd*-scaffold scale.

Methods.

Biological Material.

Virus particles. Fd viruses were grown and purified as described elsewhere.[70] Virus suspensions were then concentrated by ultracentrifugation (200 000 g) and redispersed in a stock solution of about 4 mg/mL as measured by spectrophotometry with an absorption coefficient of 3.84 cm^2/mg at 269 nm. To control the ionic conditions, the *fd* suspension was then extensively dialyzed against 10 mM sodium phosphate buffer pH 7.4 and stored at 4°C until further use.

Antibodies. The anti-*fd* polyclonal antibody (Immunoglobulin G, IgG) produced in rabbit was obtained from Sigma-Aldrich. The anti-rabbit GDH-IgG conjugate was prepared in-house by conjugating PQQ-GDH to a polyclonal goat anti-rabbit IgG, as previously detailed.[47] The anti-GDH polyclonal antibody was custom produced in rabbit by Genosphere Biotechnologies using apo-GDH monomers as antigens. The goat anti-rabbit antibody to be conjugated with GDH or Fc-PEG chains, and the bovine serum albumin (BSA) (IgG-free grade) blocking agent were from Jackson ImmunoResearch Laboratories.

Enzymes. PQQ-GDH to prepare the IgG-GDH conjugate was produced from *Acinetobacter calcoaceticus* and purified as detailed previously.[47]

Chemicals and solutions. 11-Aminoundecyltriethoxysilane (AUTES) was obtained from Alfa Aesar. All other chemicals were analytical grade Sigma-Aldrich products and used as received. All solutions were prepared with double-deionized water (18.2 MΩ cm resistivity, TKA Micro-Pure UV). Two buffer solutions were used: 10 mM phosphate buffer at pH 7.4 (phosphate buffer), and 50 mM Tris-HCl buffer at pH 7.5 (Tris buffer). Phosphate buffer was used for the preparation of the *fd* bacteriophage and of the anti-*fd* antibody solutions. Tris buffer was used to prepare the solutions of all the other antibodies, and also as the imaging medium for the in-situ AFM-SECM experiments. All antibody solutions contained 1 mg/ml BSA and 0.01 % sodium azide. Note, the stock solutions of glucose in Tris buffer were allowed to mutarotate overnight.

Preparation and characterization of the redox secondary antibody, IgG-PEG-Fc. Fc-PEG chains were covalently conjugated to goat anti-rabbit IgG by reacting the NHS activated ester of a home synthesized NHS-PEG_{3500}-Fc chain with the amino groups of the IgG species, as previously described.[58] The purified IgG-PEG-Fc is decorated with ~ 27 ± 3 Fc-PEG chains per IgG, as determined by MALDI-TOF MS.[47]

Preparation of *fd*-scaffolded integrated catalytic redox systems on SiO_2 surfaces.

Ultra-flat SiO_2 chips. The ultra-flat silicon dioxide substrates (SiO_2 chips) used to support the *fd*-scaffolded integrated systems were from NanoAndMore, and consisted of a 200 nm-thick amorphous SiO_2 layer thermally grown on a 5 x 5 mm^2 ultra-flat silicon chip.

Amino-C_{11} modified ultra-flat SiO_2 surfaces. The ultra-flat SiO_2 chip was UV-ozone cleaned for 5 min. After being rinsed with water and ethanol, it was immersed in a 1 mM 11-aminoundecyltriethoxysilane (AUTES) solution in ethanol during 30 min. AUTES was preferred over shorter chain silanes as it forms self-assembled layers on SiO_2 surfaces that are particularly stable in aqueous medium.[71] The thus obtained amino-C_{11}-silane modified chip was then thoroughly rinsed again with ethanol and water and annealed at 120 °C for 45 min. After being mounted on a 2 x 2 cm^2 glass slide with double sided tape, the chip was masked with a perforated Teflon adhesive mask to provide a 4 mm diameter disk-shaped amino-C_{11} modified ultra-flat SiO_2 surface.

Random fd arrays on SiO_2 surfaces. A 20 µL solution of phosphate buffer containing *fd* phage at 0.4 µg/mL was left on the amino-C_{11}-silane SiO_2 surface for 5 min-adsorption. The surface was then carefully rinsed by two droplet replacement steps and left in contact with phosphate buffer for 10 min to desorb any weakly bound material. These conditions yielded random arrays of irreversibly adsorbed *fd* on SiO_2 with a reproducible surface coverage of ~0.5 *fd* per μm^2. The interspace between adsorbed *fd*-particles was then backfilled with BSA protein to block non-specific binding during immune assembly steps.

Protective BSA backfilling. The *fd* arrayed-surface was then exposed to 20 µL of 2.0 mg/mL BSA in phosphate buffer solution for 1 h, followed by two subsequent rinsing and 10 min desorption steps with phosphate buffer.

Assembly of the anti-fd antibody. The *fd*-BSA backfilled surface was incubated with 20 µL of 2 µg/mL (~0.8 10^{13} molecules/mL) anti-*fd* rabbit antibody solution for 1 h, followed by two droplet replacement rinsing and desorption steps of 10 min. The surface was stored overnight at room temperature in the dark under a phosphate buffer solution containing 1 mg/ml BSA and 0.01 % (w:v) sodium azide.

Assembly of the PQQ-GDH conjugated antibody. 20 µL of a 5 µg/mL (~1.2 10^{13} molecules/mL) anti-rabbit GDH-IgG conjugate in Tris buffer was left in contact with the surface for 2 h. A double 5 min rinsing/desorption step was performed in the same buffer solution containing 1 mg/mL BSA.

Assembly of the anti-GDH antibody. The surface was then exposed to 20 µL of 5 µg/mL solution of rabbit anti-GDH IgG in Tris buffer for 1 h, rinsed by drop replacement and left to desorb twice for 5 min in Tris buffer solution with 1 mg/mL BSA.

Assembly of the IgG-PEG-Fc antibody. 20 µL of the 20 µg/mL anti-rabbit IgG-PEG-Fc solution in Tris buffer were then deposited on the surface and left to incubate overnight at 4°C under a water-saturated atmosphere. After that, 2 rinsing/desorption steps of 5 min each were carried out using Tris buffer solution with 1 mg/mL BSA.

AFM-SECM imaging. Mt/AFM-SECM images were acquired using the JPK Nanowizard II microscope operated in AFM-SECM mode as previously described.[46] The AFM-SECM tips were hand-

fabricated from flattened and etched 60 µm diameter gold microwires as detailed elsewhere.[59] For consistency, the data reported in the present paper were acquired with a limited set of tips, having similar radii of ~100 nm, spring constant in the order of 1 nN/nm, and fundamental flexural frequencies of 1-1.5 kHz. The standard JPK electrochemical liquid cell, containing 1 mL of Tris buffer, was equipped with a platinum wire counter-electrode, and a polypyrrole coated platinum wire as a quasi-reference electrode. All potentials in this work are reported *versus* a KCl saturated calomel electrode (SCE) reference. An in-house fabricated bipotentiostat was used to control the tip potential versus the reference electrode, and to measure the tip current. The tip current signal was passed through a 10 Hz low-pass analogue filter. Slow enough image scan rates (0.2-0.3 Hz) were used to avoid distortion of the current image by the filter. When needed, the tip was withdrawn a few µm away from the surface, and 100 µL of stock solutions of glucose with concentration ranging from 10 mM to 1 M were carefully injected into the liquid cell using micro-syringe equipped with a long bent metallic needle. After injection, glucose concentration was homogenized by repeatedly pumping/re-injecting ~ 100 µl of the cell solution using the micro-syringe. The tip was then brought back to the sample and the surface imaged again. The tapping mode imaging conditions were soft enough for the viral particles to be recursively imaged without being damaged by the tip. No numerical post-filtering was applied to the images, that were processed using the WSxM software.[72]

Supporting Information Available

Detailed schematic description of the step by step assembly of a random array of Fc-PEG / PQQ-GDH immunodecorated *fd* on SiO2. AFM images of the array, and analysis of topography profiles evidencing homogenous particle decoration. Variation of the height of the decorated *fd*-particles with the decoration steps. Statistical relation between the catalytic tip current of the *fd*-decorated particles and their curvature. Dependence of the particle-averaged catalytic tip current on the tip potential. Geometric modeling of the tip convolution effect on the topography and current images. Extra zoomed-in Mt/AFM-SECM images of both intact and fragmented individual decorated *fd*-particles. Derivation of the catalytic tip current profile considering the complete rate law of GDH kinetics. Tip potential dependence of current images of individual decorated *fd*-particles. This information is available free of charge on the ACS Publications website.

Acknowledgments.

Dr. Eric Grelet is warmly thanked for supplying the *fd* bacteriophage suspensions. Dr. Nicolas Mano is thanked for providing the pgp492 plasmid used to produce PQQ-GDH. We thank Drs. Benoit Limoges, François Mavré and Mathieu Branca for the generous gift of a PQQ sample. This work has received financial support from the French “Agence Nationale de la Recherche” (ANR) through “eVIRZYM” (DS0401 - ANR 2014-CE09-0009).

References

(1) Ding, S.; Cargill, A. A.; Medintz, I. L.; Claussen, J. C. Increasing the Activity of Immobilized Enzymes with Nanoparticle Conjugation. *Curr. Opin. Biotechnol.* **2015**, *34*, 242–250.

(2) Breger, J. C.; Ancona, M. G.; Walper, S. A.; Oh, E.; Susumu, K.; Stewart, M. H.; Deschamps, J. R.; Medintz, I. L. Understanding How Nanoparticle Attachment Enhances Phosphotriesterase Kinetic Efficiency. *ACS Nano* **2015**, *9*, 8491–8503.

(3) Vranish, J. N.; Ancona, M. G.; Walper, S. A.; Medintz, I. L. Pursuing the Promise of Enzymatic Enhancement with Nanoparticle Assemblies. *Langmuir* **2018**, *34*, 2901–2925.

(4) De Poulpiquet, A.; Ciaccafava, A.; Lojou, E. New Trends in Enzyme Immobilization at Nanostructured Interfaces for Efficient Electrocatalysis in Biofuel Cells. *Electrochim. Acta* **2014**, *126*, 104–114.

(5) Brown III, C. W.; Oh, E.; Hastman, D. A.; Walper, S. A.; Susumu, K.; Stewart, M. H.; Deschamps, J. R.; Medintz, I. L. Kinetic Enhancement of the Diffusion-Limited Enzyme Beta-Galactosidase When Displayed with Quantum Dots. *RSC Adv.* **2015**, *5*, 93089–93094.

(6) Algar, W. R.; Malonoski, A.; Deschamps, J. R.; Blanco-Canosa, J. B.; Susumu, K.; Stewart, M. H.; Johnson, B. J.; Dawson, P. E.; Medintz, I. L. Proteolytic Activity at Quantum Dot-Conjugates: Kinetic Analysis Reveals Enhanced Enzyme Activity and Localized Interfacial "Hopping." *Nano Lett.* **2012**, *12*, 3793–3802.

(7) Wu, M.; Algar, W. R. Acceleration of Proteolytic Activity Associated with Selection of Thiol Ligand Coatings on Quantum Dots. *ACS Appl. Mater. Interfaces* **2015**, *7*, 2535–2545.

(8) Zhao, Z.; Fu, J.; Dhakal, S.; Johnson-Buck, A.; Liu, M.; Zhang, T.; Woodbury, N. W.; Liu, Y.; Walter, N. G.; Yan, H. Nanocaged Enzymes with Enhanced Catalytic Activity and Increased Stability against Protease Digestion. *Nat. Commun.* **2016**, *7*, 10619.

(9) Zdarta, J.; Meyer, A. S.; Jesionowski, T.; Pinelo, M. A General Overview of Support Materials for Enzyme Immobilization: Characteristics, Properties, Practical Utility. *Catalysts* **2018**, *8*, 92–118.

(10) Ellis, G. A.; Klein, W. P.; Lasarte-Aragonés, G.; Thakur, M.; Walper, S. A.; Medintz, I. L. Artificial Multienzyme Scaffolds: Pursuing *in Vitro* Substrate Channeling with an Overview of Current Progress. *ACS Catal.* **2019**, *9*, 10812–10869.

(11) Müller, J.; Niemeyer, C. M. DNA-Directed Assembly of Artificial Multienzyme Complexes. *Biochem. Biophys. Res. Commun.* **2008**, *377*, 62–67.

(12) Yang, Y. R.; Liu, Y.; Yan, H. DNA Nanostructures as Programmable Biomolecular Scaffolds. *Bioconjug. Chem.* **2015**, *26*, 1381–1395.

(13) Wilner, O. I.; Weizmann, Y.; Gill, R.; Lioubashevski, O.; Freeman, R.; Willner, I. Enzyme Cascades Activated on Topologically Programmed DNA Scaffolds. *Nat Nanotechnol* **2009**, *4*, 249–254.

(14) Wilner, O. I.; Shimron, S.; Weizmann, Y.; Wang, Z. G.; Willner, I. Self-Assembly of Enzymes on DNA Scaffolds: En Route to Biocatalytic Cascades and the Synthesis of Metallic Nanowires. *Nano Lett.* **2009**, *9*, 2040–2043.

(15) Rothemund, P. W. K. Folding DNA to Create Nanoscale Shapes and Patterns. *Nature* **2006**, *440*, 297–302.

(16) Fu, J.; Liu, M.; Liu, Y.; Woodbury, N. W.; Yan, H. Interenzyme Substrate Diffusion for an Enzyme Cascade Organized on Spatially Addressable DNA Nanostructures. *J. Am. Chem. Soc.* **2012**, *134*, 5516–5519.

(17) Linko, V.; Eerikäinen, M.; Kostiainen, M. A. A Modular DNA Origami-Based Enzyme Cascade Nanoreactor. *Chem. Commun.* **2015**, *51*, 5351–5354.

(18) Fu, J.; Yang, Y. R.; Johnson-Buck, A.; Liu, M.; Liu, Y.; Walter, N. G.; Woodbury, N. W.; Yan, H. Multi-Enzyme Complexes on DNA Scaffolds Capable of Substrate Channelling with an Artificial Swinging Arm. *Nat. Nanotechnol.* **2014**, *9*, 531–536.

(19) Ke, G.; Liu, M.; Jiang, S.; Qi, X.; Yang, Y. R.; Wootten, S.; Zhang, F.; Zhu, Z.; Liu, Y.; Yang, C. J.; Yan, H. Directional Regulation of Enzyme Pathways through the Control of Substrate Channeling on a DNA Origami Scaffold. *Angew. Chemie - Int. Ed.* **2016**, *55*, 7483–7486.

(20) Ngo, T. A.; Nakata, E.; Saimura, M.; Morii, T. Spatially Organized Enzymes Drive Cofactor-Coupled Cascade Reactions. *J. Am. Chem. Soc.* **2016**, *138*, 3012–3021.

(21) Zhang, Y.; Tsitkov, S.; Hess, H. Proximity Does Not Contribute to Activity Enhancement in the Glucose Oxidase-Horseradish Peroxidase Cascade. *Nat. Commun.* **2016**, *7*, 13982.

(22) Klein, W. P.; Thomsen, R. P.; Turner, K. B.; Walper, S. A.; Vranish, J.; Kjems, J.; Ancona, M. G.; Medintz, I. L. Enhanced Catalysis from Multienzyme Cascades Assembled on a DNA Origami Triangle. *ACS Nano* **2019**, *13*, 13677–13689.

(23) Cardinale, D.; Carette, N.; Michon, T. Virus Scaffolds as Enzyme Nano-Carriers. *Trends Biotechnol.* **2012**, *30*, 369–376.

(24) Rurup, W. F.; Koay, M. S. T.; Cornelissen, J. J. L. M. Viruses as Model Nanoreactors to Study Enzyme Kinetics. In *Enzyme Nanocarriers*; Cardinale, D., Michon, T., Eds.; Taylor & Francis Group: New York, NY, 2015; pp 105–122.

(25) Patel, A. N.; Anne, A.; Chovin, A.; Demaille, C.; Grelet, E.; Michon, T.; Taofifenua, C. Scaffolding of Enzymes on Virus Nanoarrays: Effects of Confinement and Virus Organization on Biocatalysis. *Small* **2017**, *13*, 1603163.

(26) Koch, C.; Wabbel, K.; Eber, F. J.; Krolla-Sidenstein, P.; Azucena, C.; Gliemann, H.; Eiben, S.; Geiger, F.; Wege, C. Modified TMV Particles as Beneficial Scaffolds to Present Sensor

Enzymes. *Front. Plant Sci.* **2015**, *6*, 1137.

(27) Carette, N.; Engelkamp, H.; Akpa, E.; Pierre, S. J.; Cameron, N. R.; Christianen, P. C. M.; Maan, J. C.; Thies, J. C.; Weberskirch, R.; Rowan, A. E.; Nolte, R. J. M.; Michon, T.; Van Hest, J. C. M. A Virus-Based Biocatalyst. *Nat. Nanotechnol.* **2007**, *2*, 226–229.

(28) Comellas-Aragonès, M.; Engelkamp, H.; Claessen, V. I.; Sommerdijk, N. A. J. M.; Rowan, A. E.; Christianen, P. C. M.; Maan, J. C.; Verduin, B. J. M.; Cornelissen, J. J. L. M.; Nolte, R. J. M. A Virus-Based Single-Enzyme Nanoreactor. *Nat. Nanotechnol.* **2007**, *2*, 635–639.

(29) Pille, J.; Cardinale, D.; Carette, N.; Di Primo, C.; Besong-Ndika, J.; Walter, J.; Lecoq, H.; van Eldijk, M. B.; Smits, F. C. M.; Schoffelen, S.; van Hest, J. C. M.; Makinen, K.; Michon, T.; Mäkinen, K.; Michon, T. General Strategy for Ordered Noncovalent Protein Assembly on Well-Defined Nanoscaffolds. *Biomacromolecules* **2013**, *14*, 4351–4359.

(30) Patterson, D. P.; Prevelige, P. E.; Douglas, T. Nanoreactors by Programmed Enzyme Encapsulation inside the Capsid of the Bacteriophage P22. *ACS Nano* **2012**, *6*, 5000–5009.

(31) Besong-Ndika, J.; Wahlsten, M.; Cardinale, D.; Pille, J.; Walter, J.; Michon, T.; Mäkinen, K. Towards the Reconstitution of a Two-Enzyme Cascade for Resveratrol Synthesis on Potyvirus Particles. *Front. Plant Sci.* **2016**, *7*, 89.

(32) Cuenca, S.; Mansilla, C.; Aguado, M.; Yuste-Calvo, C.; Sánchez, F.; Sánchez-Montero, J. M.; Ponz, F. Nanonets Derived from Turnip Mosaic Virus as Scaffolds for Increased Enzymatic Activity of Immobilized Candida Antarctica Lipase B. *Front. Plant Sci.* **2016**, *7*, 464.

(33) Aljabali, A. A. A.; Barclay, J. E.; Steinmetz, N. F.; Lomonossoff, G. P.; Evans, D. J. Controlled Immobilisation of Active Enzymes on the Cowpea Mosaic Virus Capsid. *Nanoscale* **2012**, *4*, 5640–5645.

(34) Minten, I. J.; Claessen, V. I.; Blank, K.; Rowan, A. E.; Nolte, R. J. M.; Cornelissen, J. J. L. M.

Catalytic Capsids: The Art of Confinement. *Chem. Sci.* **2011**, *2*, 358–362.

(35) Patterson, D. P.; Schwarz, B.; Waters, R. S.; Gedeon, T.; Douglas, T. Encapsulation of an Enzyme Cascade within the Bacteriophage P22 Virus-like Particle. *ACS Chem. Biol.* **2014**, *9*, 359–365.

(36) Malanoski, A. P.; Breger, J. C.; Brown, C. W.; Deschamps, J. R.; Susumu, K.; Oh, E.; Anderson, G. P.; Walper, S. A.; Medintz, I. L. Kinetic Enhancement in High-Activity Enzyme Complexes Attached to Nanoparticles. *Nanoscale Horizons* **2017**, *12*, 3793–3802.

(37) Bollella, P.; Gorton, L. Enzyme Based Amperometric Biosensors. *Curr. Opin. Electrochem.* **2018**, *10*, 157–173.

(38) Meredith, M. T.; Minteer, S. D. Biofuel Cells: Enhanced Enzymatic Bioelectrocatalysis. *Annu. Rev. Anal. Chem.* **2012**, *5*, 157–179.

(39) Milton, R. D.; Wang, T.; Knoche, K. L.; Minteer, S. D. Tailoring Biointerfaces for Electrocatalysis. *Langmuir* **2016**, *32*, 2291–2301.

(40) Sun, L.; Gao, Y.; Xu, Y.; Chao, J.; Liu, H.; Wang, L.; Li, D.; Fan, C. Real-Time Imaging of Single-Molecule Enzyme Cascade Using a DNA Origami Raft. *J. Am. Chem. Soc.* **2017**, *139*, 17525–17532.

(41) Xu, Y.; Gao, Y.; Su, Y.; Sun, L.; Xing, F.; Fan, C.; Li, D. Single-Molecule Studies of Allosteric Inhibition of Individual Enzyme on a DNA Origami Reactor. *J. Phys. Chem. Lett.* **2018**, *9*, 6786–6794.

(42) Macpherson, J. V.; Unwin, P. R. Combined Scanning Electrochemical-Atomic Force Microscopy. *Anal. Chem.* **2000**, *72*, 276–285.

(43) Kranz, C.; Friedbacher, G.; Mizaikofft, B.; Lugstein, A.; Smoliner, J.; Bertagnolli, E. Integrating

an Ultramicroelectrode in an AFM Cantilever: Combined Technology for Enhanced Information. *Anal. Chem.* **2001**, *73*, 2491–2500.

(44) Patel, A. N.; Kranz, C. (Multi)functional Atomic Force Microscopy Imaging. *Annu. Rev. Anal. Chem.* **2018**, *11*, 329–350.

(45) Anne, A.; Chovin, A.; Demaille, C.; Lafouresse, M. High-Resolution Mapping of Redox-Immunomarked Proteins Using Electrochemical-Atomic Force Microscopy in Molecule Touching Mode. *Anal. Chem.* **2011**, *83*, 7924–7932.

(46) Nault, L.; Taofifenua, C.; Anne, A.; Chovin, A.; Demaille, C.; Besong-Ndika, J.; Cardinale, D.; Carette, N.; Michon, T.; Walter, J. Electrochemical Atomic Force Microscopy Imaging of Redox-Immunomarked Proteins on Native Potyviruses: From Subparticle to Single-Protein Resolution. *ACS Nano* **2015**, *9*, 4911–4924.

(47) Torbensen, K.; Patel, A. N.; Anne, A.; Chovin, A.; Demaille, C.; Bataille, L.; Michon, T.; Grelet, E. Immuno-Based Molecular Scaffolding of Glucose Dehydrogenase and Ferrocene Mediator on Fd Viral Particles Yields Enhanced Bioelectrocatalysis. *ACS Catal.* **2019**, *9*, 5783–5796.

(48) Takahashi, Y.; Shevchuk, A. I.; Novak, P.; Murakami, Y.; Shiku, H.; Korchev, Y. E.; Matsue, T. Simultaneous Noncontact Topography and Electrochemical Imaging by SECM/SICM Featuring Ion Current Feedback Regulation. *J. Am. Chem. Soc.* **2010**, *132*, 10118–10126.

(49) Takahashi, Y.; Shevchuk, A. I.; Novak, P.; Babakinejad, B.; Macpherson, J.; Unwin, P. R.; Shiku, H.; Gorelik, J.; Klenerman, D.; Korchev, Y. E.; Matsue, T. Topographical and Electrochemical Nanoscale Imaging of Living Cells Using Voltage-Switching Mode Scanning Electrochemical Microscopy. *Proc. Natl. Acad. Sci. U. S. A.* **2012**, *109*, 11540–11545.

(50) Mirkin, M. V; Sun, T.; Yu, Y.; Zhou, M. Electrochemistry at One Nanoparticle. *Acc. Chem. Res.* **2016**, *49*, 2328–2335.

(51) Sun, T.; Zhang, H.; Wang, X.; Liu, J.; Xiao, C.; Nanayakkara, S. U.; Blackburn, J. L.; Mirkin, M. V.; Miller, E. M. Nanoscale Mapping of Hydrogen Evolution on Metallic and Semiconducting MoS2 Nanosheets. *Nanoscale Horizons* **2019**, *4*, 619–624.

(52) Bentley, C. L.; Kang, M.; Unwin, P. R. Nanoscale Structure Dynamics within Electrocatalytic Materials. *J. Am. Chem. Soc.* **2017**, *139*, 16813–16821.

(53) Kang, M.; Perry, D.; Bentley, C. L.; West, G.; Page, A.; Unwin, P. R. Simultaneous Topography and Reaction Flux Mapping at and around Electrocatalytic Nanoparticles. *ACS Nano* **2017**, *11*, 9525–9535.

(54) Bentley, C. L.; Unwin, P. R. Nanoscale Electrochemical Movies and Synchronous Topographical Mapping of Electrocatalytic Materials. *Faraday Discuss.* **2018**, *210*, 365–379.

(55) Bentley, C. L.; Edmondson, J.; Meloni, G. N.; Perry, D.; Shkirskiy, V.; Unwin, P. R. Nanoscale Electrochemical Mapping. *Anal. Chem.* **2019**, *91*, 84–108.

(56) Pouget, E.; Grelet, E.; Lettinga, M. P. Dynamics in the Smectic Phase of Stiff Viral Rods. *Phys. Rev. E - Stat. Nonlinear, Soft Matter Phys.* **2011**, *84*, 41704.

(57) Zimmermann, K.; Hagedorn, H.; Heuck, C. C.; Hinrichsen, M.; Ludwig, H. The Ionic Properties of the Filamentous Bacteriophages Pf1 and Fd. *J. Biol. Chem.* **1986**, *261*, 1653–1655.

(58) Anne, A.; Demaille, C.; Moiroux, J. Elastic Bounded Diffusion. Dynamics of Ferrocene-Labeled Poly(ethylene Glycol) Chains Terminally Attached to the Outermost Monolayer of Successively Self-Assembled Monolayers of Immunoglobulins. *J. Am. Chem. Soc.* **1999**, *121*, 10379–10388.

(59) Abbou, J.; Demaille, C.; Druet, M.; Moiroux, J. Fabrication of Submicrometer-Sized Gold Electrodes of Controlled Geometry for Scanning Electrochemical-Atomic Force Microscopy. *Anal. Chem.* **2002**, *74*, 6355–6363.

(60) Kuznetsov, Y. G.; McPherson, A. Atomic Force Microscopy in Imaging of Viruses and Virus-Infected Cells. *Microbiol. Mol. Biol. Rev.* **2011**, *75*, 268–295.

(61) Anne, A.; Demaille, C.; Moiroux, J. Elastic Bounded Diffusion and Electron Propagation: Dynamics of the Wiring of a Self-Assembly of Immunoglobulins Bearing Terminally Attached Ferrocene Poly(ethylene Glycol) Chains according to a Spatially Controlled Organization. *J. Am. Chem. Soc.* **2001**, *123*, 4817–4825.

(62) Chidsey, C. E. D.; Bertozzi, C. R.; Putvinski, T. M.; Mujsce, A. M. Coadsorption of Ferrocene-Terminated and Unsubstituted Alkanethiols on Gold: Electroactive Self-Assembled Monolayers. *J. Am. Chem. Soc.* **1990**, *112*, 4301–4306.

(63) Gonçales, V. R.; Lian, J.; Gautam, S.; Tilley, R. D.; Gooding, J. J. Functionalized Silicon Electrodes in Electrochemistry. *Annu. Rev. Anal. Chem.* **2020**, *13*.

(64) Edwards, G. A.; Bergren, A. J.; Porter, M. D. 8 - Chemically Modified Electrodes; Zoski, C. G. B. T.-H. of E., Ed.; Elsevier: Amsterdam, 2007; pp 295–327.

(65) Blauch, D. N.; Savéant, J. M. Dynamics of Electron Hopping in Assemblies of Redox Centers. Percolation and Diffusion. *J. Am. Chem. Soc.* **1992**, *114*, 3323–3332.

(66) Abbou, J.; Anne, A.; Demaille, C. Accessing the Dynamics of End-Grafted Flexible Polymer Chains by Atomic Force-Electrochemical Microscopy. Theoretical Modeling of the Approach Curves by the Elastic Bounded Diffusion Model and Monte Carlo Simulations. Evidence for Compression-Induced Late. *J. Phys. Chem. B* **2006**, *110*, 22664–22675.

(67) Abbou, J.; Anne, A.; Demaille, C. Probing the Structure and Dynamics of End-Grafted Flexible Polymer Chain Layers by Combined Atomic Force-Electrochemical Microscopy. Cyclic Voltammetry within Nanometer-Thick Macromolecular Poly(ethylene Glycol) Layers. *J. Am. Chem. Soc.* **2004**, *126*, 10095–10108.

(68) Durand, F.; Limoges, B.; Mano, N.; Mavré, F.; Miranda-Castro, R.; Savéant, J. M. Effect of Substrate Inhibition and Cooperativity on the Electrochemical Responses of Glucose Dehydrogenase. Kinetic Characterization of Wild and Mutant Types. *J. Am. Chem. Soc.* **2011**, *133*, 12801–12809.

(69) Zhang, L.; Miranda-Castro, R.; Stines-Chaumeil, C.; Mano, N.; Xu, G.; Mavré, F.; Limoges, B. Heterogeneous Reconstitution of the PQQ-Dependent Glucose Dehydrogenase Immobilized on an Electrode: A Sensitive Strategy for PQQ Detection down to Picomolar Levels. *Anal. Chem.* **2014**, *86*, 2257–2267.

(70) Sambrook, J.; Fritsch, E. F.; Maniatis, T. *Molecular Cloning: A Laboratory Manual.*; New-York, 1989, pp 38-41.

(71) Giraud, L.; Nadarajah, R.; Matar, Y.; Bazin, G.; Sun, J.; Zhu, X. X.; Giasson, S. Amino-Functionalized Monolayers Covalently Grafted to Silica-Based Substrates as a Robust Primer Anchorage in Aqueous Media. *Appl. Surf. Sci.* **2016**, *370*, 476–485.

(72) Horcas, I.; Fernández, R.; Gómez-Rodríguez, J. M.; Colchero, J.; Gómez-Herrero, J.; Baro, A. M. WSXM: A Software for Scanning Probe Microscopy and a Tool for Nanotechnology. *Rev. Sci. Instrum.* **2007**, *78*, 13705.

Graphical Table of Contents